An elaborate dynamic model of dual-motor precision transmission mechanism for performance optimization

Jieji Zheng (zhengjieji@nudt.edu.cn)
National University of Defense Technology College of Mechatronic Engineering and Automation
Ruoyu Tan
National University of Defense Technology College of Intelligence Science
Baoyu LI
National University of Defense Technology College of Intelligence Science
Dapeng Fan
National University of Defense Technology College of Intelligence Science
Xin Xie
National University of Defense Technology College of Intelligence Science https://orcid.org/0000-0002-3017-2319

Research Article

Keywords: Dual-motor precision transmission mechanism, Detailed linear model, Dead-zone, Friction

Posted Date: May 27th, 2022

DOI: https://doi.org/10.21203/rs.3.rs-1546754/v1

Title page

An elaborate dynamic model of dual-motor precision transmission mechanism for performance optimization

Jieji Zheng, born in 1993, is currently a PhD at *Mechanical Engineering in the college of intelligence science and technology, National University of Defense Technology, China.* He received the bachelor degree from Central South University, China, in 2016 and the master degree from National University of Defense Technology, China, in 2018, respectively. His current research focuses on electromechanical servo system control.
Tel: +86-187-11124584; E-mail: zhengjieji@nudt.edu.cn

Ruoyu Tan, born in 1990, is currently a PhD at *Mechanical Engineering in the college of intelligence science and technology, National University of Defense Technology, China.*
E-mail: tanruoyu17@nudt.edu.cn

Baoyu Li, born in 1991, is currently a PhD at *Mechanical Engineering in the college of intelligence science and technology, National University of Defense Technology, China.*
E-mail: lbyu@nudt.edu.cn

Dapeng Fan, born in 1964, is currently a professor at *National University of Defense Technology, China*. He received his PhD degree from *National University of Defense Technology, China*, in 1991. His research interests include mechachonics engineering, Electromechanical Servo System and Precision drive transmission.
Tel: +86-138-07480956; E-mail: fdp@nudt.edu.cn

Xin Xie, born in 1991, is currently an assistant researcher at *National University of Defense Technology, China*. He received his PhD degree from *National University of Defense Technology, China*, in 2019. His research interests include mechachonics engineering, Electromechanical Servo System and Precision drive transmission.
Tel: +86-137-87043604; E-mail: xiexin12@nudt.edu.cn

Corresponding author： Xin Xie E-mail： xiexin12@nudt.edu.cn

ORIGINAL ARTICLE

An elaborate dynamic model of dual-motor precision transmission mechanism for performance optimization

Jie-Ji Zheng[1] • Ruo-Yu Tan[1] • Bao-Yu Li[1] • Da-Peng Fan[1] • Xin Xie[1]

Received June xx, 201x; revised February xx, 201x; accepted March xx, 201x

Abstract: The dual-motor precision transmission mechanism (DMPTM) is an alternative way to eliminate backlash completely while ensuring the stiffness of the servo system. However, most of the established models of DMPTM are not accurate enough, which are not conducive to the optimization of system performance and the design of high-precision controllers. In this paper, based on the detailed linear model of the single components of the DMPTM, the dead zone model considering the time-varying stiffness is proposed to describe the backlash of the two transmission chain and the friction of the mechanism is depicted by Stribeck model. Then, a high-precision dynamic model of the DMPTM is formed. Finally, the model validation experiments of the open-loop and closed-loop are carried out in the time domain and frequency domain. The experimental results show that the proposed model can accurately describe the nonlinear characteristics of the mechanism. The Pearson correlation coefficient between the proposed model and the actual system is $r_{\text{open-loop}}$ >99.41% for open-loop and $r_{\text{closed-loop}}$ >83.7% for closed-loop, which are both better than the existing model. In the frequency domain, whether it is open-loop or closed-loop, the frequency response of the proposed model also reproduces the actual system well, which verifies the accuracy of the model.

Keywords: Dual-motor precision transmission mechanism • Detailed linear model • Dead-zone • Friction

✉ Xin Xie
xiexin12@nudt.edu.cn

[1] Mechanical Engineering in the college of intelligence science and technology, National University of Defense Technology, Changsha, 410073, China.

1 Introduction

Inertially stabilized platforms (ISPs) have been widely used in precision pointing mechanisms such as remote control weapon stations, tracking radars, optical imaging equipment, antennas, and telescopes[1–5], to isolate the influence of base disturbances on pointing accuracy. As the load of ISPs increases, a torque amplification device must be added to drive the load for high dynamic response. Due to the compact space of the azimuth platform of ISPs, the traditional reducer with a large reduction ratio cannot meet the volume requirements, so the two-stage transmission mode of the planetary reducer and the large ring gear(LRG) in series is still irreplaceable. However, due to the large diameter of the LRG, it is difficult to ensure the manufacturing accuracy of the teeth, resulting in an unpredictable meshing backlash between the gears. Backlash not only deteriorates the control accuracy, reduce the bandwidth, cause limit cycle oscillation, but also give rise to nonlinear dynamic response, such as frequency jump, chaos and bifurcation[6–12].

For this problem, scholars have proposed various solutions to eliminate backlash. Among them, using the dual-motor precision transmission mechanism(DMPTM) is receiving more and more attention. By applying equal and opposite bias torques to the two sets of motors, it can theoretically eliminate backlash completely while ensuring the stiffness of the servo system[13–16], that is a distinctive superiority of DMPTM. However, the DMPTM complicates the kinetic properties of ISPs and makes the analysis of the system properties difficult. Up to now, most of the models of DMPTM directly simplify the DMPTM to

a three-inertia mechanism and apply the traditional dead-zone model to describe the particularity of backlash[17–20], which are not conducive to the optimization of system performance. The reason is that the traditional dead zone model does not really reflect the system backlash characteristics and the nonlinearity of friction is ignored.

Backlash has a serious impact on system performance and lots of mathematical models for backlash and gear play have been published. Ref.[21] reviewed the progress in nonlinear dynamics of gear driven systems in the past twenty years, especially the gear dynamic behaviour considering the backlash. Guesalaga A[10] established a backlash model using the "bristle" approach. The model introduces a continuous hysteresis representation, different from classical discontinuous models, showing a behaviour closer to what has been observed empirically. Merzouki R[22] modelled disturbing backlash torque by a continuous and derivable mathematical function describing an opposite of sigmoid function. Barbosa RS[23] and Duarte FB[24] analyse the dynamical properties of systems with backlash and impact phenomena based on the describing function method. While the describing function has the defect of can only be used for frequency domain stability analysis. The deadzone model[25, 26] is the most widely used to depict backlash in the time domain. Due to the non-differentiable property of the traditional deadzone model, which makes the control design problem very complex and difficult, Shi Z[27] proposes a “soft degree” concept based on a recently developed differentiable deadzone model, and then presents a practical backstepping algorithm to achieve not only high-precision output tracing but also limit cycles elimination. Yongjun S[28, 29] considered the time-varying stiffness on the basis of the dead zone model when studying the nonlinear dynamics of the gear pair based on the incremental harmonic balance method. Based on the results presented in his paper the periodic solution with arbitrary precision can be expeditiously obtained, which is useful in analysing or controlling the dynamics of the gear system. A shortcoming of the studies above is that the non-contact area is regarded as no output by ignoring the influence of viscous damping, which cause the backlash characteristics cannot be truly reflected. Aiming at this phenomenon, Kranawetter K[30] and Nordin M[31] proposed a new dead zone model based on phase plane analysis, which takes into account the damping of gears in the non-contact phase and corrects the boundary of the non-contact area. The accuracy of the models is improved and provides a reference for the backlash analysis in this paper, but they do not give consideration to the friction nonlinearity of the gears.

In summary, the existing research on the accurate modelling of the transmission chain in the field of the DMPTM has not yet seen relevant reports. When studying the nonlinearity of backlash, friction is not given enough attention, resulting in a comparatively large deviation from the actual system.

In order to improve the control accuracy of the system, the system must be deeply analysed. Therefore, an elaborate dynamic model of the DMPTM needs to be established. Given the above, the single components of the DMPTM have been detailed modelled. On the basis of the linear model assembled in this way, a dead zone model considering the time-varying mesh stiffness is put forward and the Stribeck model is used to describe the friction nonlinearity. Thereby, a complete nonlinear dynamic model of the DMPTM is formed.

The following contributions can thus be identified in this paper: (1) A case-study of the complex transmission chain of the DMPTM is worked out in detail; (2) The time-varying stiffness is premeditated in the dead zone model.

The organization of this study is as follows. The detailed linear model of the transmission chain of the DMPTM is established in Section 2., while the dead zone model considering the time-varying stiffness and the friction model of the system are established in Section 3. Then the accuracy of the proposed model is experimentally verified in the time domain and frequency domain through Section 4. Finally, the conclusion of this study is summarized in Section 5.

2 Component modelling

2.1 Overall structure of the DMPTM

The system presented in this paper is shown in Figure 1. The structure of a typical DMPTM is sketched in Figure 1, which consists of two identical transmission chains (including a permanent magnet synchronous motor (PMSM), a L-shaped planetary reducer (LSPR) and a pinion) and a LRG.

First of all, a detailed linear model of the DMPTM has been derived, which reveals the torque transmission principle of the mechanism. In this process, it is necessary to identify the degrees of freedom that mostly contribute to the exchange of the mechanical actions. Basically, the degrees of freedom included in the model are those that are directly implied by the transmission of the torque from the motor to the last stage of the transmission. Details on

modelling the single components are reported in the following subsections.

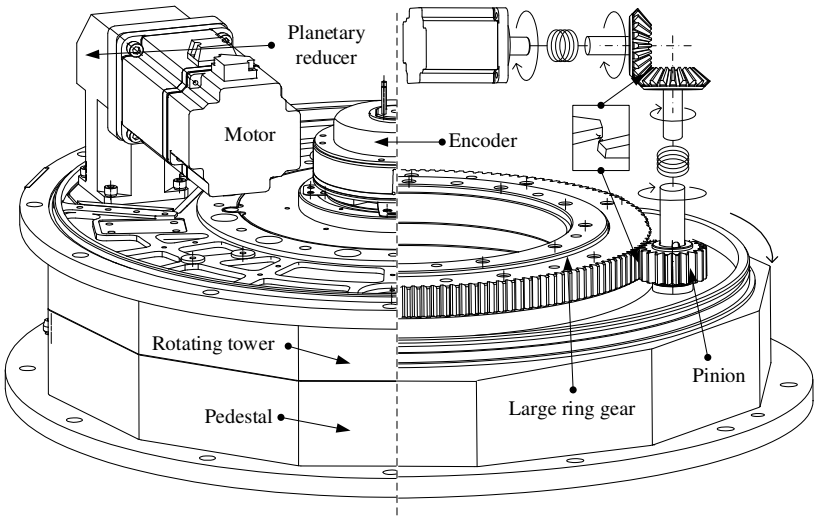

Figure 1 Schematic diagram of the transmission structure of the DMPTM

2.2 Motor and driving wheel of LSPR

Figure 2 shows the coupling between the motor and the driving wheel of the LSPR, whose equations are easily derived as a two-mass compliant system:

$$J_m\ddot{\theta}_0 + D_m\dot{\theta}_0 = T_m - T_{01} \tag{1}$$

$$J_1\ddot{\theta}_1 + D_1\dot{\theta}_1 = T_{01} - F_{12t}R_1 \tag{2}$$

$$T_m = \mathrm{K_d}\mathrm{K_M}u \tag{3}$$

$$T_{01} = K_{01}\Delta\theta_{01} \tag{4}$$

$$\Delta\theta_{01} = \theta_0 - \theta_1 \tag{5}$$

where J_m, D_m are the inertia and damping of the motor rotor while J_1, D_1 are the inertia and damping of the driving wheel of the LSPR; θ_0, θ_1 are the rotation angle of the motor rotor and the driving wheel respectively; K_{01} is the stiffness of the motor shaft; T_m, T_{01} are the electromagnetic torque of the motor and the input torque of the LSPR respectively; $\mathrm{K_d}$ is the amplification factor of the driver while $\mathrm{K_M}$ is the torque constant of the motor; u is the input voltage of the motor; F_{12t} is the circumferential force of the driving wheel; R_1 is the radius of the driving wheel.

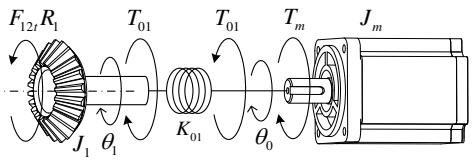

Figure 2 Motor and the driving wheel of LSPR coupling

2.3 Internal bevel gear drive of LSPR

The first-stage deceleration of the transmission chain is realized by the LSPR. Figure 3 shows the bevel gear transmission inside the reducer. The dynamic equation of the LSPR is:

$$J_2\ddot{\theta}_2 + D_2\dot{\theta}_2 = F_{12t}\cdot R_2 - T_{23} \tag{6}$$

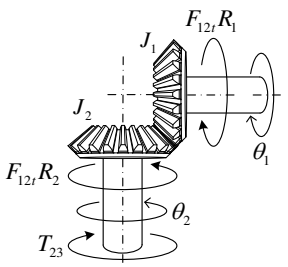

Figure 3 Bevel gear meshing transmission of the LSPR

where J_2, D_2 are the inertia and damping of the driven wheel of the LSPR; R_2 is the radius of the driven wheel; T_{23} is the output torque of the LSPR; The force analysis of the bevel gear teeth is shown in Figure 4, and the circumferential force F_{12t} and normal force F_{12n} when the gear teeth are meshed can be obtained as follows:

$$F_{12t} = F_{12n}\cos\alpha_1 \tag{7}$$

$$F_{12n} = K_{12}\Delta L_{12} + D_{12}\Delta\dot{L}_{12} \tag{8}$$

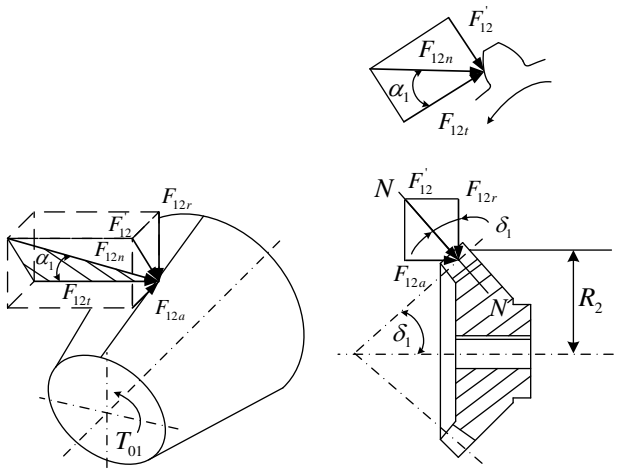

Figure 4 Force analysis of bevel gear teeth

where α_1 is the pressure angle of the bevel gear, K_{12}, D_{12} are the meshing stiffness and meshing damping of the bevel gear, respectively; ΔL_{12} is the deformation of the teeth of the bevel gear. Figure 5 shows the relative motion of gear meshing and the deformation ΔL_{12} can be expressed by Eq. (9):

$$\Delta L_{12} = (\theta_1 R_1 - \theta_2 R_2)\cos\alpha_1 \cos\delta_1 \tag{9}$$

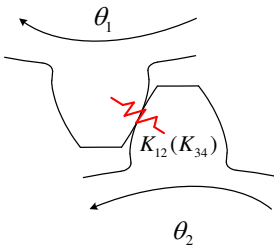

Figure 5 Relative motion of gear meshing

where δ_1 is the taper angle of the bevel gear

2.4 Driven wheel of LSPR and pinion

The coupling of the driven wheel of the LSPR to the pinion is shown in Figure 6, and the dynamic equation can be described as:

$$J_3\ddot{\theta}_3 + D_3\dot{\theta}_3 = T_{23} - F_{34t}R_3 \tag{10}$$

$$T_{23} = K_{23}\Delta\theta_{23} \tag{11}$$

$$\Delta\theta_{23} = \theta_2 - \theta_3 \tag{12}$$

$$F_{34t} = (K_{34}\Delta L_{34} + D_{34}\Delta\dot{L}_{34})\cos\alpha_3 \tag{13}$$

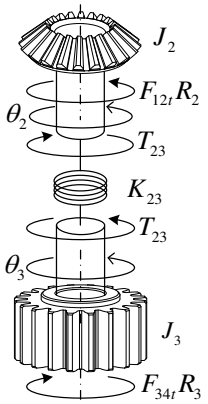

Figure 6 Coupling between the driven wheel of the LSPR and the pinion

where J_3, D_3 are the inertia and damping of the pinion while K_{23} is the stiffness of the output shaft; θ_2, θ_3 are the rotation angle of the driven wheel and the pinion respectively; F_{34t} is the circumferential force of the pinion and R_3 is the radius of the pinion; K_{34}, D_{34} are the meshing stiffness and meshing damping of the pinion respectively; α_3 is the pressure angle of the gear and ΔL_{34} is the deformation of the teeth of the gears. The deformation ΔL_{34} can be expressed by Eq. (14):

$$\Delta L_{34} = (\theta_3 R_3 - \theta_L R_L)\cos\alpha_3 \tag{14}$$

where θ_L, R_L are the rotation angle and the radius of the LRG, respectively.

2.5 Pinions and LRG

Figure 7 shows a schematic diagram of the coupling between one of the pinions and the LGR, and Figure 8 shows the meshing dynamics model of the two pinions

and the LGR. By analysing Figure 7 and Figure 8, the dynamic equation of the LGR can be obtained as:

$$\begin{aligned} J_L\ddot{\theta}_L + D_L\dot{\theta}_L &= F_{l34t}R_L + F_{r34t}R_L \\ &= (K_{34}\Delta L_{l34} + D_{34}\Delta\dot{L}_{l34})R_L\cos\alpha_3 \\ &\quad + (K_{34}\Delta L_{r34} + D_{34}\Delta\dot{L}_{r34})R_L\cos\alpha_3 \end{aligned} \tag{15}$$

where J_L, D_L are the inertia and damping of the LRG; F_{l34t}, F_{r34t} are the circumferential forces of the LGR on both sides; $\Delta L_{l34}, \Delta L_{r34}$ are the deformations of the teeth of the gears.

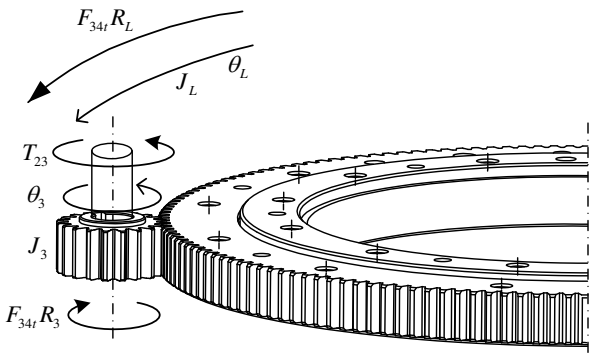

Figure 7 Pinion and LGR coupling

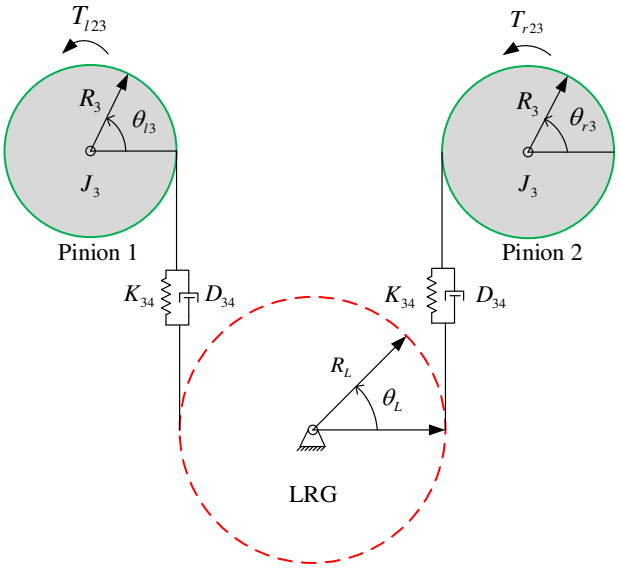

Figure 8 Dynamic model of meshing two pinions with the LGR

2.6 Overall linear model

The equations derived above are all linear, forming a detailed linear model of the overall transmission chain of the DMPTM, which can be represented by Figure 9.

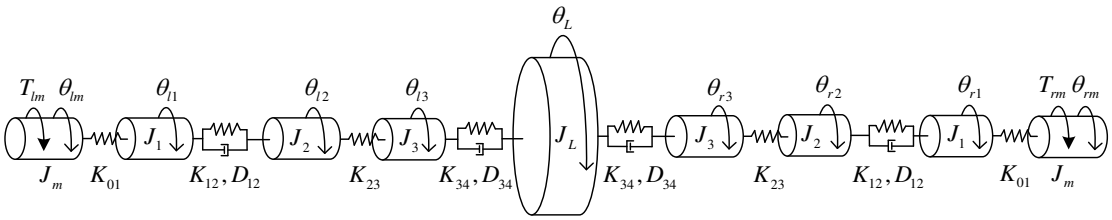

Figure 9 Overall linear model of the DMPTM

The model depicted in Figure 9 contains 9 degrees of freedom, resulting in a very complex model. In order to analyse the factors that have a greater impact on the system performance inside the system, we can find ways to simplify the model reasonably. The rigidity of the motor shaft is large enough and the backlash of the LSPRs are within 7arcmin. Moreover, the internal detailed parameters of the LSPRs are not convenient to obtain since they form proprietary background of the manufacturer of the transmission. Hence, the motors and the LSPRs can be regarded as ideal transmission links, so $\theta_{lm} \approx \theta_{l1}, \theta_{rm} \approx \theta_{r1}, \theta_{l2} \approx \theta_{l3}, \theta_{r2} \approx \theta_{r3}$ are obtained. The relationship from the motor angle to the pinion angle can be simplified as:

$$\theta_{lm} \approx N_1\theta_{l3}, \theta_{rm} \approx N_1\theta_{r3} \tag{16}$$

where N_1 is the reduction ratio of the LSPR. The simplified overall linear model of the system is shown in Figure 10.

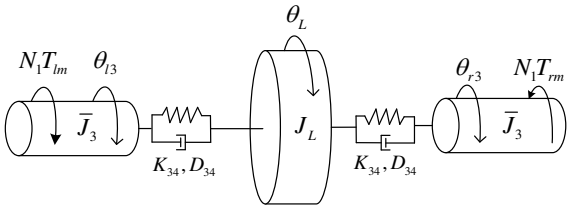

Figure 10 Simplified overall linear model of the DMPTM

where $\bar{J}_3 = N_1^2J_m + J_1 + J_2 + J_3$ in the figure is the sum of the inertia equivalent to the pinion end. The simplified system vibration equation is shown in Eq. (17):

$$\bar{M}\ddot{\bar{X}} + \bar{D}\dot{\bar{X}} + \bar{K}\bar{X} = \bar{E}T \tag{17}$$

where

$$\bar{E}^T = \begin{bmatrix} N_1 & 0 & 0 \\ 0 & N_1 & 0 \end{bmatrix}$$
$$\bar{X}^T = \begin{bmatrix} \theta_{l3} & \theta_{r3} & \theta_L \end{bmatrix}$$
$$\bar{M} = diag\begin{bmatrix} \bar{J}_3 & \bar{J}_3 & J_L \end{bmatrix}$$

See the appendix for the expression of matrix $\bar{D}$ and $\bar{K}$. Neglecting the effect of damping in the vibration equation, the Eq. (17) can be simplified to an undamped free vibration equation:

$$\bar{M}\ddot{\bar{X}} + \bar{K}\bar{X} = \bar{E}T \tag{18}$$

Therefore, the resonant frequency ω_{NTF} of the system satisfies:

$$\bar{K} - \omega_{NTF}^2 \bar{M} = 0 \tag{19}$$

Substitute $\bar{M}$ and $\bar{K}$ into formula (19) to get the determinant:

$$\det \begin{vmatrix} \bar{k}_{1,1} - \omega_{NTF}^2 \bar{J}_3 & 0 & \bar{k}_{1,3} \\ 0 & \bar{k}_{2,2} - \omega_{NTF}^2 \bar{J}_3 & \bar{k}_{2,3} \\ \bar{k}_{3,1} & \bar{k}_{3,2} & \bar{k}_{3,3} - \omega_{NTF}^2 J_L \end{vmatrix} = 0 \tag{20}$$

The system resonance frequency can be obtained by solving Eq. (20).

3 Analysis of nonlinear dynamics

The two identical transmission chains of the DMPTM consist of two stages. The first stage is a LSPR (backlash <7arcmin) and the effect of the backlash on the system after deceleration can be ignored, but its friction becomes an important factor. The second stage consists of a pinion and a LRG, whose manufacturing and assembly errors making the meshing backlash large, which will directly affect the servo performance of the system. At the same time, the friction of the LRG is also a key factor affecting the performance of the system.

On the basis of the detailed linear model established in Section 2, a dead zone model considering the time-varying stiffness is established to depict the backlash between the pinion and the LRG. Furthermore, the Stribeck model is adopted to describe the friction of the two LSPRs and the LRG.

3.1 Dead zone model

The backlash of gears is shown in Figure 11, and 2Δ in the figure represent the backlash. According to Ref.[30], the dead zone model of the pinion gear and the LRG can be expressed by Eq. (21):

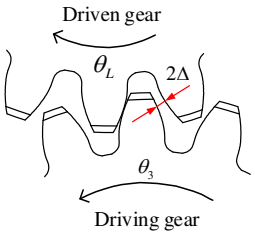

Figure 11 Backlash of gears

$$\tau_c = \begin{cases} k(z-\Delta) + c\dot{z} & (z,\dot{z}) \in A^+ \\ c_f \dot{z} & (z,\dot{z}) \in A_0 \\ k(z+\Delta) + c\dot{z} & (z,\dot{z}) \in A^- \end{cases} \tag{21}$$

where

$$A^+ = \{(z,\dot{z}):$$
$$\left\{ \begin{array}{ll} z - \dfrac{c_f}{k}\dot{z} + \dfrac{c+c_f}{k}\dot{z}e^{-\frac{k}{c+c_f}\left(\frac{z+b}{\dot{z}}+\frac{c}{k}\right)} \geq \Delta, \dot{z} > 0 \\ k(z-\Delta) + c\dot{z} \geq 0, & \forall \dot{z} \end{array} \right\}$$
$$A^- = \{(z,\dot{z}):$$
$$\left\{ \begin{array}{ll} z - \dfrac{c_f}{k}\dot{z} + \dfrac{c+c_f}{k}\dot{z}e^{-\frac{k}{c+c_f}\left(\frac{z-b}{\dot{z}}+\frac{c}{k}\right)} \leq -\Delta, \dot{z} < 0 \\ k(z-\Delta) + \dot{z} \leq 0, & \forall \dot{z} \end{array} \right\}$$
$$A_0 = \{(z,\dot{z})\} \setminus (A^+ \cup A^-)$$

where k and c are meshing stiffness and meshing damping, respectively; $z = \theta_3 - N_2\theta_L = \theta_3 - \frac{z_L}{z_3}\theta_L$ is the transmission error between the pinion and the LRG, while z_3, z_L are the number of teeth of the pinion and the LRG, respectively; c_f is the damping when the pinion and the LRG is in a non-contact state.

The meshing stiffness k in the teeth engagements (between the pinion gear and the LRG) has been computed making reference to a simplified scheme of the tooth, sketched in Figure 12. The tooth is represented as a clamped bracket with variable section and with the force applied to the pitch circle of the wheel. The stiffness of the tooth has been computed with the formula:

$$k=\left(\int_0^{h_1}\frac{x^2}{EJ(x)}dx\right)^{-1} \tag{22}$$

where h_1 is the distance from the base of the tooth to the pitch circle of the tooth; x is the linear coordinate along the distance, and $J(x)$ is the polar moment of inertia of the section. For the specific calculation process of $J(x)$, please refer to Ref.[32].

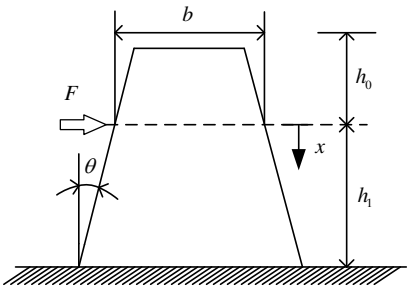

Figure 12 Scheme of the tooth profile

Convert k to the meshing stiffness in the circumferential direction of the gear as the gear meshing average stiffness k_m. The time-varying mesh stiffness $k(t)$ of gear meshing can be expressed by Eq. (23)[33]:

$$k(t)=k_m+k_a\cos\left(\omega_z t+\varphi_r\right) \tag{23}$$

where k_a is the variable stiffness amplitude; ω_z is the variable stiffness fundamental frequency, and $\omega_z=2\pi n_3 z_3/60$; n_3 is the pinion speed; φ_r is the variable stiffness phase angle, generally taken as $\varphi_r=0$.

The meshing damping of gears can be expressed by Eq. (24)[33]:

$$c=2\zeta\sqrt{\frac{k_{\mathrm{m}}R_3^2R_L^2J_3J_L}{R_3^2J_3+R_L^2J_L}} \tag{24}$$

where ζ is the damping ratio, which is taken as 0.03-0.17.

3.2 Stribeck friction model

The frictions of the system are all represented by the Stribeck model, and its expression is as follows:

$$\mathbf{T}_{\mathrm{f}}\left(\dot{\theta},\mathbf{T}_{\mathrm{m}}\right)=\begin{cases}\mathbf{T}_{\mathrm{m}},\ \text{if}\ \left(\dot{\theta}=0\ \text{and}\ \mathbf{T}_{\mathrm{s}}^{-}<\mathbf{T}_{\mathrm{m}}<\mathbf{T}_{\mathrm{s}}^{+}\right)\\ \mathbf{T}_{\mathrm{s}}^{+},\text{if}\ \left(\dot{\theta}=0\ \text{and}\ \mathbf{T}_{\mathrm{m}}>\mathbf{T}_{\mathrm{s}}^{+}\right)\\ \mathbf{T}_{\mathrm{s}}^{-},\text{if}\ \left(\dot{\theta}=0\ \text{and}\ \mathbf{T}_{\mathrm{m}}<\mathbf{T}_{\mathrm{s}}^{-}\right)\\ \mathbf{T}_{\mathrm{C}}^{+}+\left(\mathbf{T}_{\mathrm{s}}^{+}-\mathbf{T}_{\mathrm{c}}^{+}\right)\mathrm{e}^{-(\dot{\theta}/\Omega_{+})^{\delta}}+B^{+}\dot{\theta},\ \text{if}\ (\dot{\theta}>0)\\ \mathbf{T}_{\mathrm{C}}^{-}+\left(\mathbf{T}_{\mathrm{s}}^{-}-\mathbf{T}_{\mathrm{c}}^{-}\right)\mathrm{e}^{-(\dot{\theta}/\Omega_{-})^{\delta}}+B^{-}\dot{\theta},\ \text{if}\ (\dot{\theta}<0)\end{cases} \tag{25}$$

where $\mathbf{T}_{\mathrm{f}}$ is the friction torque; $\mathbf{T}_{\mathrm{s}}^{+},\mathbf{T}_{\mathrm{s}}^{-}$ are the static friction torques; $\mathbf{T}_{\mathrm{c}}^{+},\mathbf{T}_{\mathrm{c}}^{-}$ are the Coulomb friction torques; Ω_{+}, Ω_{-} are the Stribeck velocities; δ is an empirical constant; B^{+}, B^{-} are the viscous damping.

The detailed linear model of the system established in Section 2 and the dead zone model and friction model are integrated to form the nonlinear dynamic model of the DMPTM, as shown in Figure 13. In the figure, T_{f1},T_{f2},T_{fL} are the friction of the two LSPRs and the LRG, while Δ_1,Δ_2 are the meshing backlash between the two pinions and the LRG, respectively.

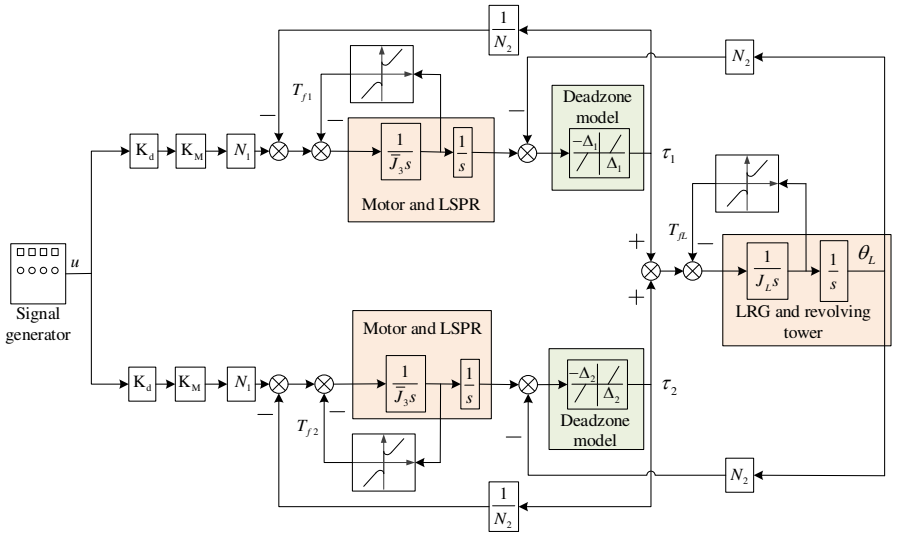

Figure 13 Block diagram of the nonlinear dynamic model of the DMPTM

4 Model validation

4.1 Experimental setup

A DMPTM experimental device as shown in Figure 14 was built, mainly consisting of two PMSMs (model: SPALY80), two drivers (model: Elmo P/N: SOL-WHI 20/100PYE), two LSPRs (model: FABR060-25-S2-P1), an azimuth platform, an absolute encoder (model: CAPRO-B112050), a fiber optic gyroscope (model: FOG-118), a 24V power supply, a 48V power supply, dSPACE1104 and industrial computer.

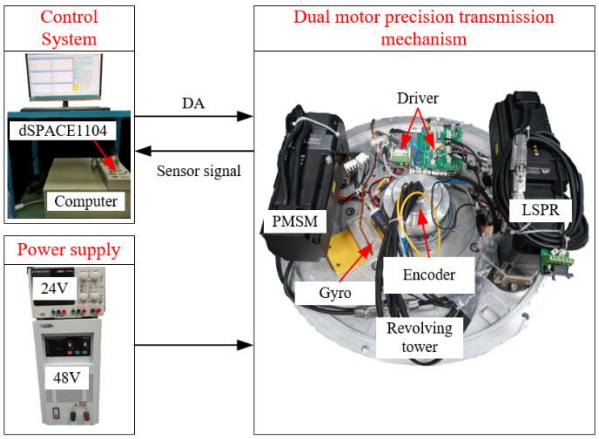

Figure 14 Experimental device for the test of the DMPT

4.2 Determination of model parameters

The kinetic model worked out so far involve many mechanical parameters, whose accurate knowledge is essential. An analysis has been performed in order to derive expressions for these parameters in terms of geometrical properties of the bodies, and properties (inertial and elastic ones) of the materials. This analysis is briefly summarized hereafter.

4.2.1 Inertia parameter

The acquisition of inertia parameters is relatively simple. The inertia of the motor and reducer is directly provided by the manufacturer, and the inertia of the pinion gear, the LRG and the rotating tower can be calculated by a solid modeller.

4.2.2 Dead zone model parameters

The parameters that need to be obtained for the dead zone model mainly include the size Δ_1, Δ_2 of the meshing backlash between the two pinions and the LRG teeth and the dead zone transition damping c_f.

The value of Δ_1, Δ_2 is mainly obtained through the experimental test. In this paper, the reverse motion measurement method is used to obtain the Δ_1, Δ_2 through the difference between the forward and reverse rotation angles. Dead zone transition damping c_f is an adjustable parameter, and takes a value with a higher degree of fitting with the measured data.

4.2.3 Friction model parameters

The Stribeck friction models of the LSPRs and the LRG have been obtained through standard identification experiments and are not reported here for brevity.

By consulting the parameters provided by the equipment manufacturer and the test results, the system parameter values shown in Table 1 are obtained. Table 2 shows the friction model parameters of the LSPRs and the LRG.

Table 1 System parameter values

Symbol	Value	Symbol	Value
$K_d(A \cdot V^{-1})$	3	z_3	20
$K_M(N \cdot m \cdot A^{-1})$	0.13	z_L	165
$J_m(kg \cdot m^2)$	2×10^{-4}	$k_m(N \cdot m \cdot rad^{-1})$	3.6×10^4
$J_2(kg \cdot m^2)$	0.125	$c(N \cdot m \cdot rad^{-1} \cdot s)$	1
$J_L(kg \cdot m^2)$	2.5	Δ_1(arcmin)	14
N_1	25	Δ_2(arcmin)	10
N_2	8.25		

Table 2 Friction model parameter values

Friction of the LSPRs		Friction of the LRG	
Symbol	Value	Symbol	Value
$\mathbf{T}_{3s}^{+}(N \cdot m)$	2.5	$\mathbf{T}_{Ls}^{+}(N \cdot m)$	23
$\mathbf{T}_{3s}^{-}(N \cdot m)$	-2	$\mathbf{T}_{Ls}^{-}(N \cdot m)$	-20
$\mathbf{T}_{3c}^{+}(N \cdot m)$	2.8	$\mathbf{T}_{Lc}^{+}(N \cdot m)$	20
$\mathbf{T}_{3c}^{-}(N \cdot m)$	-1.8	$\mathbf{T}_{Lc}^{-}(N \cdot m)$	-17
$\Omega_{3+}(deg \cdot s^{-1})$	2	$\Omega_{L+}(deg \cdot s^{-1})$	1
$\Omega_{3-}(deg \cdot s^{-1})$	-2	$\Omega_{L-}(deg \cdot s^{-1})$	-1
δ_3	1	δ_L	1
$B_3^{+}(N \cdot m \cdot deg^{-1} \cdot s)$	0.01	$B_L^{+}(N \cdot m \cdot deg^{-1} \cdot s)$	1.2
$B_3^{-}(N \cdot m \cdot deg^{-1} \cdot s)$	0.008	$B_L^{-}(N \cdot m \cdot deg^{-1} \cdot s)$	1

4.3 Experimental results

In order to fully verify the accuracy of the model, the model response and the actual system response when the system is open-loop and closed-loop are compared in the time domain and frequency domain, respectively. Reference will be made to the velocity control loop (Figure 15), the loop is closed on the load side, the speed

measurements being actually numerical differentiations of position measurements obtained with an encoder. A PI (Proportional Integral) regulator $G_c(s) = k_p + k_i \frac{1}{s}$ is used, whose tuning had already been performed independently of this analysis. This tuning, however, is inessential here, as the goal is just the validation of the model.

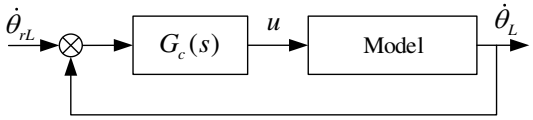

Figure 15 PI speed control system

In the figure, $\dot{\theta}_{rL}$ is the velocity setpoint, and $\dot{\theta}_L$ is the velocity response of the LRG.

4.3.1 Open loop time response

First, the open-loop time-domain responses of the system are verified experimentally. Apply different excitation signals to the motor, and the comparison results are shown in Figure 16(a)~Figure 16(d). In the figure, the red solid lines are the model established according to the existing method of Ref.[17–20], the blue solid lines are the model proposed in this paper, and the black dotted lines are the response of the actual system. It can be seen from the comparison results that the fitting degrees of the proposed model and the actual system are higher than that of the existing model, no matter under the excitation of sinusoidal signals or square wave signals with different amplitudes and frequencies. The proposed model can better reproduce the zero-crossing dead-zone characteristics and the transition time of commutation of the actual system, which are the key factors affecting the performance of the servo system.

4.3.2 Open loop frequency response

In the frequency domain, the frequency responses of the model and the system at different voltage amplitudes are also contrasted, and the results are shown in Figure 17(a) and Figure 17(b). The results show that the amplitude and phase of the proposed model fit the system frequency response characteristics better than the existing model as well.

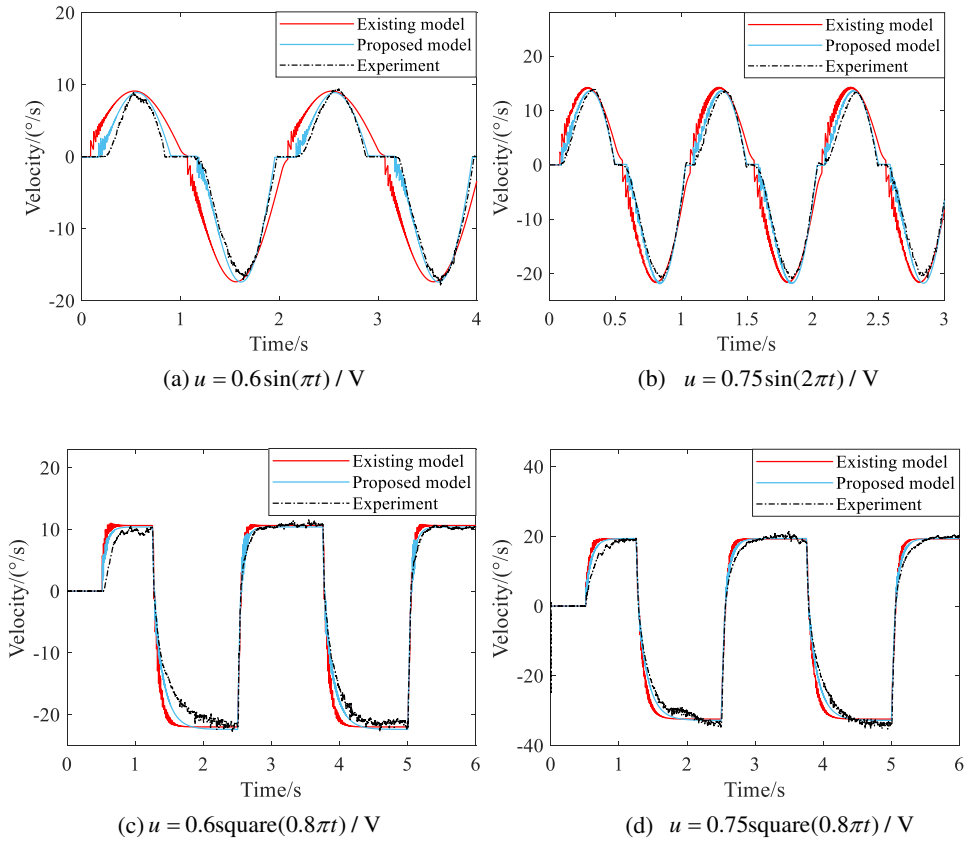

(a) $u = 0.6\sin(\pi t)$ / V (b) $u = 0.75\sin(2\pi t)$ / V

(c) $u = 0.6\text{square}(0.8\pi t)$ / V (d) $u = 0.75\text{square}(0.8\pi t)$ / V

Figure 16 Simulated and experimental time responses under open-loop

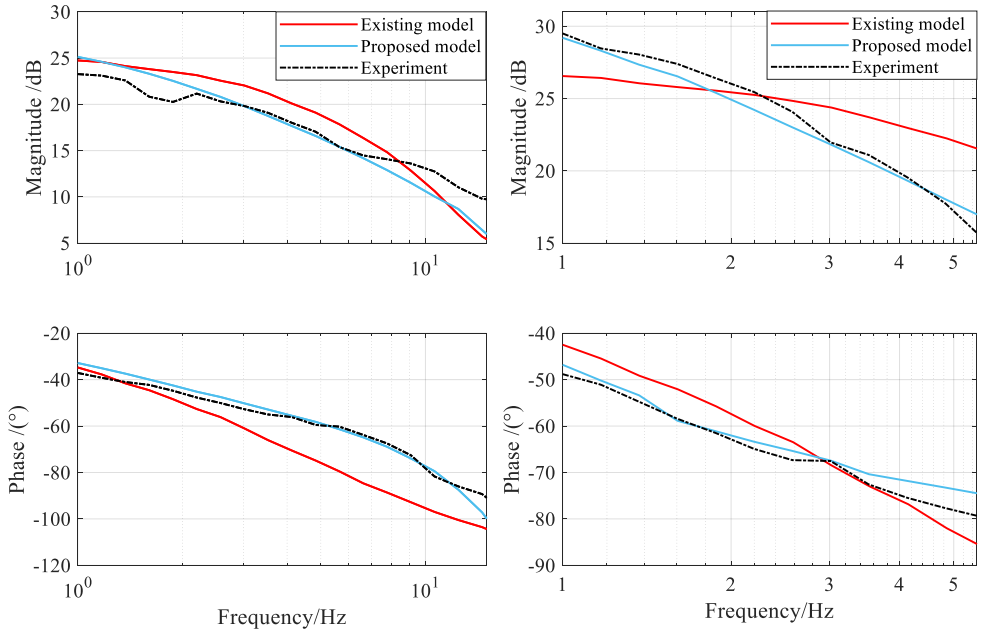

(a) $u_{amplitude} = 0.75$ / V (b) $u_{amplitude} = 1.5$ / V

Figure 17 Simulated and experimental frequency responses under open-loop

4.3.3 Closed loop time response

After adding the closed-loop PI regulator, a further set of experiments have been conducted in order to test the ability of the model in reproducing the response of the system to setpoints. The comparison results shown in Figure 18(a)~Figure 18(d) also reveal that the proposed model is much better than the existing model. The proposed model can accurately reproduce the zero-crossing dead zone and velocity fluctuation when following a sinusoidal signal, as well as the overshoot and oscillation times when following a square wave, while the existing model cannot.

4.3.4 Closed loop frequency response

In the frequency domain, the closed-loop frequency responses of the model and the system at different speed command amplitudes are compared, and the results are shown in Figure 19(a) and Figure 19(b). The comparison results show that the proposed model accurately reproduces the system frequency response in terms of amplitude and phase. In particular, the 5.5Hz resonance point after the system is closed is well captured, which shows that the backlash and friction nonlinearity of the system lead to a low bandwidth, that is not conducive to the high dynamic control of ISPs. However, the existing model cannot reproduce the closed-loop frequency domain characteristics of the system.

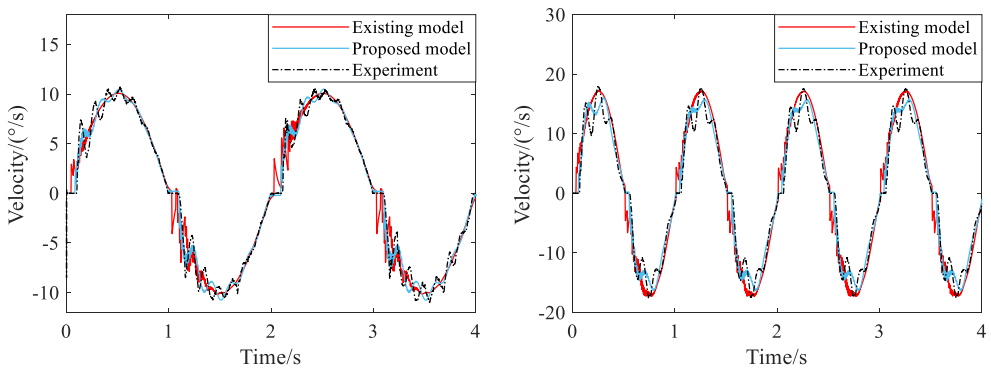

(a) $\dot{\theta}_{rL} = 10\sin(\pi t)$ / (°/s) (b) $\dot{\theta}_{rL} = 15\sin(2\pi t)$ / (°/s)

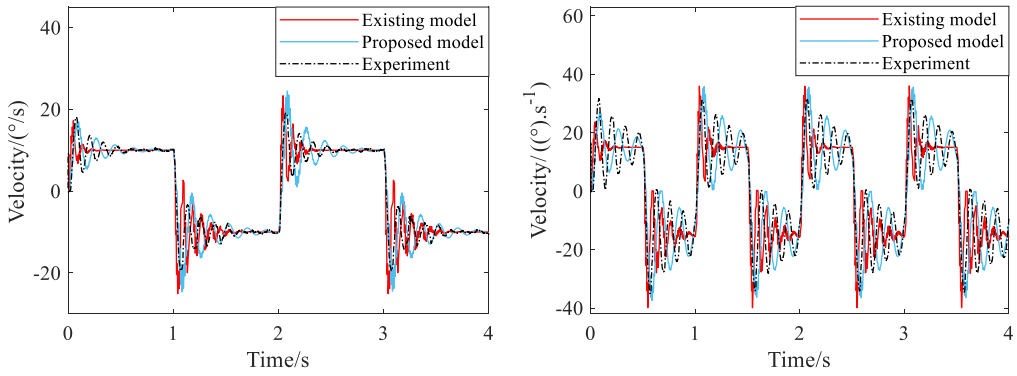

(c) $\dot{\theta}_{rL}=10\text{square}(\pi t)/(°/\text{s})$　　(d) $\dot{\theta}_{rL}=15\text{square}(2\pi t)/(°/\text{s})$

Figure 18 Simulated and experimental time responses under closed-loop

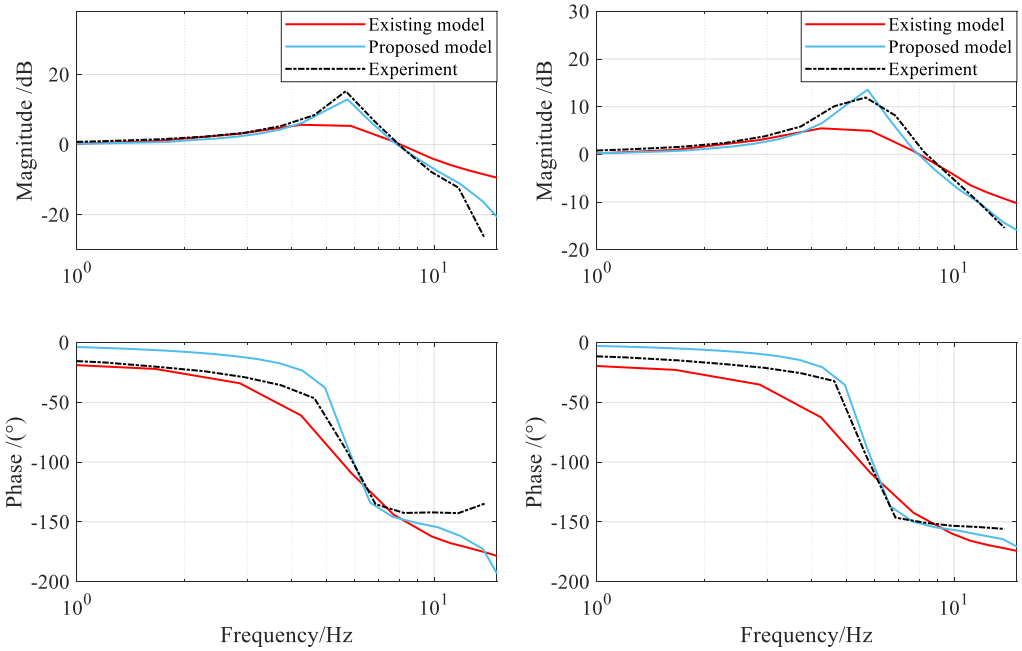

(a) $\dot{\theta}_{rL\_amplitude}=10/(°/\text{s})$　　(b) $\dot{\theta}_{rL\_amplitude}=15/(°/\text{s})$

Figure 19 Simulated and experimental frequency responses under closed-loop

In order to quantify the accuracy of the model, the Pearson correlation coefficient was used to evaluate the fitting degree of the model response curve and the actual response curve. The Pearson correlation coefficient are calculated according to Figure 16 and Figure 18, as shown in Table 3 and Table 4. From the results, it can be seen that the fitting degree between the proposed model and the actual is $r_{\text{open-loop}}$ >99.41% for open-loop and $r_{\text{closed-loop}}$ >83.7% for closed-loop, which verifies the accuracy of the model. Compared with the existing model, it can be improved by up to 5.61% and 1.78% in open-loop and closed-loop, respectively.

Table 3 The Pearson correlation coefficient for open-loop time responses

Experiments	Existing model /%	Proposed model /%	Improvement /%
(a) $0.6\sin(\pi t)/\text{V}$	94.13	99.41	5.61
(b) $0.75\sin(2\pi t)/\text{V}$	97.47	99.67	2.26
(c) $0.6\text{square}(0.8\pi t)/\text{V}$	99.14	99.68	0.54
(d) $0.75\text{square}(0.8\pi t)/\text{V}$	99.30	99.73	0.43

Table 4 The Pearson correlation coefficient for closed-loop time responses

Experiment	Existing model /%	Proposed model /%	Improvement /%
(a) $10\sin(\pi t)$ / (°/s)	98.53	99.17	0.65
(b) $15\sin(2\pi t)$ / (°/s)	98.13	98.66	0.54
(c) $10\text{square}(\pi t)$ / (°/s)	92.77	94.42	1.78
(d) $15\text{square}(2\pi t)$ / (°/s)	82.75	83.70	1.15

5 Conclusions

(1) High performance control of ISPs can be achieved provided that a reasonable knowledge of the dynamic model of the mechanical system is available. In this paper, the single components of the transmission chain are introduced in detail. Then the overall linear dynamic model of the DMPTM is formed.

(2) In the nonlinear aspects of the system, the dead-zone model considering the time-varying stiffness is proposed to describe the system backlash and the Stribeck model is used to analyse the friction of the system.

(3) The experimental results in the time-domain show that the proposed model are highly consistent with the actual system. The fitting degree between the model and the actual speed response is $r_{\text{open-loop}}$ >99.41% for open-loop and $r_{\text{closed-loop}}$ >83.7% for closed-loop, which are better than the existing model.

(4) In the frequency domain, whether it is under the open-loop or the closed-loop, the fitting degree is very good, verifying the accuracy of the proposed model.

(5) The research of this paper can provide a theoretic guide for the optimization of system performance and the design of high-precision controllers.

6 Declaration

Acknowledgements

The authors sincerely thanks to Professor Dapeng Fan of National University of Defense Technology University for his critical discussion and reading during manuscript preparation.

Funding

Supported by National Key R&D Program of China (Grant No. 2019YFB2004700).

Availability of data and materials

The datasets supporting the conclusions of this article are included within the article.

Authors' contributions

The author' contributions are as follows: Jieji Zheng was in charge of the whole trial and wrote the manuscript; Ruoyu Tan and Baoyu Li assisted with sampling and laboratory analyses; Da-Peng Fan provided funding acquisition and reviewed the manuscript; Xin Xie reviewed and edited the manuscript;

Competing interests

The authors declare no competing financial interests.

Consent for publication

Not applicable

Ethics approval and consent to participate

Not applicable

References

[1] Konigseder F, Kemmetmuller W, Kugi A. Attitude Estimation Using Redundant Inertial Measurement Units for the Control of a Camera Stabilization Platform. IEEE Trans Control Syst Technol ,2016, 24:1837–1844

[2] Zhou X, Shi Y, Li L, Yu R, Zhao L. A High Precision Compound Control Scheme Based on Non-singular Terminal Sliding Mode and Extended State Observer for an Aerial Inertially Stabilized Platform. Int J Control Autom Syst ,2020, 18:1498–1509

[3] Azarskov V, Tunik A, Sushchenko O, Pourtakdoust SH. Design of Composite Feedback and Feedforward Control Law for Aircraft Inertially Stabilized Platforms. Int J Aerosp Eng, 2020, 1–9

[4] Jiang X, Fan D, Fan S, Xie X, Chen N. High-precision gyro-stabilized control of a gear-driven platform with a floating gear tension device. Front Mech Eng, 2021, 16:487–503

[5] Li S, Zhong M. High-Precision Disturbance Compensation for a Three-Axis Gyro-stabilized Camera Mount. IEEEASME Trans Mechatron, 2015, 20:3135–3147

[6] Walha L, Fakhfakh T, Haddar M. Backlash effect on dynamic analysis of a two-stage spur gear system. J Fail Anal Prev, 2006, 6:60–68

[7] Dwivedula RV, Pagilla PR. Effect of Compliance and Backlash on the Output Speed of a Mechanical Transmission System. J Dyn Syst Meas Control , 2012, 134

[8] Adlene R, Abderrazak L. Study on the influence of backlash phenomenon on wind turbine power using bond graph approach. J Braz Soc Mech Sci Eng , 2018, 40:91

[9] Yang X, Lu D, Liu S, Zhang J, Zhao W. Modeling and analysis of steady-state vibration induced by backlash in servo rotary table. Front Mech Eng , 2015, 10:43–47

[10] Guesalaga A. Modelling end-of-roll dynamics in positioning servos. Control Eng Pract , 2004, 12:217–224

[11] Wang C, Yang M, Zheng W, Hu K, Xu D. Analysis and Suppression of Limit Cycle Oscillation for Transmission System With Backlash Nonlinearity. IEEE Trans Ind Electron, 2017, 64:9261–9270

[12] Yang M, Wang C, Xu D, Zheng W, Lang X. Shaft Torque Limiting

Control Using Shaft Torque Compensator for Two-Inertia Elastic System With Backlash. IEEEASME Trans Mechatron , 2016, 21:2902–2911

[13] Wang B, Iwasaki M, Yu J. Command filtered adaptive backstepping control for dual-motor servo systems with torque disturbance and uncertainties. IEEE Trans Ind Electron , 2021, 1–1.

[14] Lee H, Choi Y. A New Actuator System Using Dual-Motors and a Planetary Gear. IEEEASME Trans Mechatron , 2012, 17:192–197

[15] Gawronski W, Beech-Brandt JJ, Ahlstrom HG, Maneri E. Torque-bias profile for improved tracking of the Deep Space Network antennas. IEEE Antennas Propag Mag, 2000, 42:35–45

[16] Zhao W, Ren X, Gao X. Synchronization and tracking control for multi-motor driving servo systems with backlash and friction: SYNCHRONIZATION AND TRACKING CONTROL FOR MULTI-MOTOR. Int J Robust Nonlinear Control , 2016, 26:2745–2766

[17] Zhao W, Ren X, Li L. Synchronization and Tracking Control for Dual‐motor Driving Servo Systems with Friction Compensation. Asian J Control, 2019, 21:674‐685

[18] Wen C. Modelling and Simulation of Dual-Pinion Driving Systems for Backlashes Elimination. Int J Model Simul , 2010, 30:178–158

[19] Zeng T, Ren X, Zhang Y. Fixed-Time Sliding Mode Control and High-Gain Nonlinearity Compensation for Dual-Motor Driving System. IEEE Trans Ind Inform , 2020, 16:4090–4098

[20] Zeng T, Ren X, Zhang Y. Fixed-time sliding mode control based plant/controller co-design of dual-motor driving system. Int J Syst Sci , 2019, 50:1847–1859

[21] Wang J, Li and R, Peng X. Survey of nonlinear vibration of gear transmission systems. Appl Mech Rev , 2003, 56:309–329

[22] Merzouki R, Cadiou JC. Estimation of backlash phenomenon in the electromechanical actuator. Control Eng Pract, 2005, 13:973–983

[23] Barbosa RS, Machado JAT Describing Function Analysis of Systems with Impacts and Backlash. Nonlinear Dyn , 2002, 29:235–250

[24] Duarte FB, Machado JT. Describing function of two masses with backlash. Nonlinear Dyn , 2008, 56:409

[25] Kahraman A, Singh R. NON-LINEAR DYNAMICS OF A SPUR GEAR PAIR. J Sound Vib , 1990, 99:1227–1241

[26] Villwock S, Pacas M. Time-Domain Identification Method for Detecting Mechanical Backlash in Electrical Drives. IEEE Trans Ind Electron , 2009, 1982 56:568–573

[27] Shi Z, Zuo Z. Backstepping Control for Gear Transmission Servo Systems With Backlash Nonlinearity. IEEE Trans Autom Sci Eng , 2015, 12:752–757

[28] Yongjun S, Shaopu Y, Cunzhi P, Xiandong L. Nonlinear Dynamics of a Spur Gear Pair with Time-Varying Stiffness and Backlash. J Low Freq Noise Vib Act Control, 2004, 23:179–187

[29] Shen Y, Yang S, Liu X. Nonlinear dynamics of a spur gear pair with time-varying stiffness and backlash based on incremental harmonic balance method. Int J Mech Sci , 2006, 48:1256–1263

[30] Kranawetter K, Seeber R, Bauer R, Horn M. A New Backlash and Gear Play Model with Friction. IEEE, pp , 2019, 346–351

[31] Nordin M, Galic J, Gutman P-O. New models for backlash and gear play. Int J Adapt Control Signal Process , 1997, 11:49–63

[32] Magnani G, Rocco P. Mechatronic analysis of a complex transmission chain for performance optimization in a machine tool. Mechatronics, 2010, 20:85–101

[33] Li Runfang, Wang Jianjun. Gear System Dynamics: Vibration, Shock, Noise. Gear System Dynamics: Vibration, Shock, Noise, 1997(in Chinese)

Biographical notes

Jieji Zheng, born in 1993, is currently a PhD at *Mechanical Engineering in the college of intelligence science and technology, National University of Defense Technology, China.* He received the bachelor degree from Central South University, China, in 2016 and the master degree from National University of Defense Technology, China, in 2018, respectively. His current research focuses on electromechanical servo system control.
Tel: +86-187-11124584; E-mail: zhengjieji@nudt.edu.cn

Ruoyu Tan, born in 1990, is currently a PhD at *Mechanical Engineering in the college of intelligence science and technology, National University of Defense Technology, China.*
E-mail: tanruoyu17@nudt.edu.cn

Baoyu Li, born in 1991, is currently a PhD at *Mechanical Engineering in the college of intelligence science and technology, National University of Defense Technology, China.*
E-mail: lbyu@nudt.edu.cn

Dapeng Fan, born in 1964, is currently a professor at *National University of Defense Technology, China*. He received his PhD degree from *National University of Defense Technology, China*, in 1991. His research interests include mechachonics engineering, Electromechanical Servo System and Precision drive transmission.
Tel: +86-138-07480956; E-mail: fdp@nudt.edu.cn

Xin Xie, born in 1991, is currently an assistant researcher at *National University of Defense Technology, China*. He received his PhD degree from *National University of Defense Technology, China*, in 2019. His research interests include mechachonics engineering, Electromechanical Servo System and Precision drive transmission.
Tel: +86-137-87043604; E-mail: xiexin12@nudt.edu.cn

Appendix

$$\bar{D}=\begin{bmatrix}\bar{d}_{1,1} & 0 & \bar{d}_{1,3}\\ 0 & \bar{d}_{2,2} & \bar{d}_{2,3}\\ \bar{d}_{3,1} & \bar{d}_{3,2} & \bar{d}_{3,3}\end{bmatrix},\bar{K}=\begin{bmatrix}\bar{k}_{1,1} & 0 & \bar{k}_{1,3}\\ 0 & \bar{k}_{2,2} & \bar{k}_{2,3}\\ \bar{k}_{3,1} & \bar{k}_{3,2} & \bar{k}_{3,3}\end{bmatrix}$$

where

$$\bar{d}_{1,1} = D_3 + D_{34} R_3^2 C_{34}$$
$$\bar{d}_{1,3} = \bar{d}_{3,1} = -D_{34} R_3 R_4 C_{34}$$
$$\bar{d}_{2,2} = D_3 + D_{34} R_3^2 C_{34}$$
$$\bar{d}_{2,3} = \bar{d}_{3,2} = -D_{34} R_3 R_4 C_{34}$$
$$\bar{d}_{3,3} = D_L + 2D_{34} R_4^2 C_{34}$$
$$\bar{k}_{1,1} = K_{34} R_3^2 C_{34}$$
$$\bar{k}_{1,3} = \bar{k}_{3,1} = -K_{34} R_3 R_4 C_{34}$$
$$\bar{k}_{2,2} = K_{34} R_3^2 C_{34}$$
$$\bar{k}_{2,3} = \bar{k}_{3,2} = -K_{34} R_3 R_4 C_{34}$$
$$\bar{k}_{3,3} = 2K_{34} R_4^2 C_{34}$$
$$C_{12} = \cos^2 \alpha_1 \cos \delta_1$$
$$C_{34} = \cos^2 \alpha_3$$